Nanoscale Res Lett (2010) 5:263–273
DOI 10.1007/s11671-009-9445-0

NANO EXPRESS

Synthesis and Cytotoxicity of Y_2O_3 Nanoparticles of Various Morphologies

Tamar Andelman · Simon Gordonov · Gabrielle Busto · Prabhas V. Moghe · Richard E. Riman

Received: 8 June 2009 / Accepted: 24 September 2009 / Published online: 24 November 2009

Abstract As the field of nanotechnology continues to grow, evaluating the cytotoxicity of nanoparticles is important in furthering their application within biomedicine. Here, we report the synthesis, characterization, and cytotoxicity of nanoparticles of different morphologies of yttrium oxide, a promising material for biological imaging applications. Nanoparticles of spherical, rod-like, and platelet morphologies were synthesized via solvothermal and hydrothermal methods and characterized by transmission electron microscopy (TEM), X-ray diffraction (XRD), light scattering, surface area analysis, thermogravimetric analysis (TGA), and zeta potential measurements. Nanoparticles were then tested for cytotoxicity with human foreskin fibroblast (HFF) cells, with the goal of elucidating nanoparticle characteristics that influence cytotoxicity. Cellular response was different for the different morphologies, with spherical particles exhibiting no cytotoxicity to HFF cells, rod-like particles increasing cell proliferation, and platelet particles markedly cytotoxic. However, due to differences in the nanoparticle chemistry as determined through the characterization techniques, it is difficult to attribute the cytotoxicity responses to the particle morphology. Rather, the cytotoxicity of the platelet sample appears due to the stabilizing ligand, oleylamine, which was present at higher levels in this sample. This study demonstrates the importance of nanoparticle chemistry on in vitro cytotoxicity, and highlights the general importance of thorough nanoparticle characterization as a prerequisite to understanding nanoparticle cytotoxicity.

Keywords Yttrium oxide · Y_2O_3 · Nanoparticle synthesis · Nanoparticle toxicity · Morphology control

T. Andelman · R. E. Riman (✉)
Department of Materials Science & Engineering, Rutgers The State University of New Jersey, 607 Taylor Road, Piscataway, NJ 08854, USA
e-mail: riman@rci.rutgers.edu

T. Andelman · S. Gordonov · G. Busto · P. V. Moghe · R. E. Riman
Department of Biomedical Engineering, Rutgers The State University of New Jersey, 599 Taylor Road, Piscataway, NJ 08854, USA

P. V. Moghe
Department of Chemical and Biochemical Engineering, Rutgers The State University of New Jersey, 98 Brett Road, Piscataway, NJ 08854, USA

Introduction

Interest in nanoparticles for biological and medical applications continues to grow. Nanoparticles find use as delivery vehicles for drugs [1, 2], genes [3, 4], and growth factors [5], as well as cellular labels for imaging both in vitro and in vivo [6–8]. Nanoparticles are also being studied for use in photodynamic therapy (PDT) [9] and hyperthermia therapy for tumors [10], with the goal of clinical applications. Organic nanoparticles, such as polymeric or protein nanoparticles, and inorganic nanoparticles, such as gold and semiconductor nanoparticles, are being investigated for these applications. Clearly, for any biological or medical application of nanoparticles, biocompatibility of the nanoparticles is imperative.

Nanoparticles can disrupt and impair normal cellular function through a number of different mechanisms [11]. First, nanoparticles may be comprised of toxic materials or ions that poison the cells, or materials that generate free radicals, such as reactive oxygen species (ROS). For example, some metal and semiconductor nanoparticles,

such as CdSe or CdTe, are known to be cytotoxic to a variety of cells [12, 13]. This is in part due to material decomposition and release of toxic Cd^{2+} ions, which bind to sulfohydryl groups of mitochondria protein, causing mitochondrial dysfunction and cellular poisoning [14]. Material decomposition is of greater likelihood for nanoparticles than bulk material due to their enhanced surface area to volume ratio. Generation of free radicals following excitation and photooxidation of CdTe nanoparticles has also been observed to contribute to cytotoxicity [15]. Cytotoxicity due to ROS generation has been reported with a number of different nanoparticles, including TiO_2 [16], C_{60} [17], and CeO_2 [18]. Second, regardless of composition, the nanoparticles may adhere to cell membranes or pass through the membrane and become internalized within the cell, which may impair cellular functions [11, 19]. For example, charged nanoparticles enter cells through the creation of pores in the cellular membrane [20], a phenomenon associated with cytotoxicity. Third, the morphology of the nanoparticle may disrupt the cellular membrane, as in the case of carbon nanotubes that have reportedly speared cells like lancets, killing them [21, 22].

Altering nanoparticle characteristics such as size, surface chemistry, phase, and morphology can tune the earlier mentioned cytotoxicity mechanisms, potentially resulting in greatly different cytotoxicity responses for materials of essentially the same composition. For example, CdTe nanoparticles of different sizes display different degrees of cytotoxicity, due in part to differences in cellular uptake and cell internalization pathways, which are dictated by size [23]. Polystyrene nanoparticles functionalized with NH_2 on their surface were markedly more cytotoxic than bare polystyrene nanoparticles or COOH-functionalized polystyrene nanoparticles, due to increased cellular uptake [24]. Anatase phase TiO_2 nanoparticles are reportedly 100 times more toxic than equivalent size and shape rutile phase TiO_2 nanoparticles, due to changes in exposed surface atoms which render the anatase phase more efficient at generation of ROS [25]. Carbon nanoparticles of different morphologies (spheres, multiwalled spheres, nanotubes, multiwalled nanotubes) were found to have different degrees of cytotoxicity [26, 27]. It was concluded from these results that the cells responded differently according to the shape of the nanomaterials. In another study, spherical Au nanoparticles were not found to be toxic to human skin cells, while Au nanorods synthesized from the Au nanoparticles via a seed mediated, surface assisted growth method were observed to be highly toxic [28]. Whether the nanoscale geometry plays a role here was not clear, as this was attributed to the presence of hexadecylcetlytrimethylammonium bromide (CTAB), a surfactant used to stabilize the nanorods that is not present on the nanoparticles. A study of Pt nanoparticles of different morphologies reported that surface area and oxidant reactivity of certain morphologies increased cellular uptake ($\sim$1.5 times greater) and increased retention in lung tissue when compared to other morphologies [29]. In fact, surface area was highlighted as being an important nanoparticle characteristic for studying and predicting the toxicology of nanoparticles by The European Centre for Ecotoxicology and Toxicology of Chemicals [30].

In light of these studies, we report here on the synthesis and characterization of various yttrium oxide nanoparticle morphologies to assess cytotoxicity and reactive oxygen species (ROS) generation, with the aim of determining the nanoparticle characteristics that are important in designing biocompatible nanoparticles. Such correlations are currently lacking for yttrium oxide nanoparticles. We hypothesize that different yttrium oxide powder characteristics will have different cytotoxicity responses and different ROS generation levels and that characterization will reveal the specific nanoparticle characteristics that govern the cytotoxicity responses in this system.

Yttrium oxide, Y_2O_3, a widely used host material for various rare earth dopants, is of interest for potential applications in biological imaging, as well as photodynamic therapy [31–33]. Yttrium and the rare earth element commonly doped (Yb, Er, Eu) into yttrium oxide are not known to be cytotoxic, making yttrium oxide a better candidate than the quantum spherical nanoparticle chemistries for in vivo applications. Cubic phase yttrium oxide possesses a low phonon energy of 380 cm^{-1}, which makes it a good host for upconversion, i.e., emission of a lower wavelength photon, such as in the visible range, upon excitation with a longer wavelength photon, typically in the near infrared (NIR) range [34–36]. This is of particular interest in biological imaging, as the main absorbers in tissue, namely water, hemoglobin, and melanin, have minimal absorption in the NIR [37]. Thus, use of nanoparticles with excitation in the NIR wavelengths would allow for deeper penetration of excitation photons for deep tissue imaging applications. Additionally, it has been reported that monoclinic yttrium oxide nanoparticles can protect cells from oxidative stress [38]; however, this has not been studied with cubic phase Y_2O_3, which possesses superior upconversion properties and is therefore of greater interest for biological imaging applications [39].

Yttria and yttrium oxide precursors have been prepared by a number of synthetic methods. Combustion synthesis has been used by different groups to prepare nanoparticles and nanocrystalline powders of yttrium oxide [35, 40–43]. Solvothermal and hydrothermal synthesis [44–48], precipitation techniques [49–55], and thermal decomposition methods [56, 57] are also widespread methods for preparation of Y_2O_3. A variety of nanoparticle morphologies for yttrium oxide, including spherical nanoparticles [58–61], nanorods [59], nanowires [47], nanotubes [48, 62], and

nanodisks [56, 57], have been synthesized from different methods. Morphological control over Y_2O_3 nanoparticles has been achieved with hydrothermal synthesis by varying pH, but the resulting nanorods and nanoflakes had lengths and lateral dimensions, respectively, on the order of microns [62]. Wire-like and spherical morphologies of Y_2O_3 were synthesized by a solvothermal method by varying solvent composition [47]. Zhang et al. [59] reported morphological evolution of spherical nanoparticles into nanorods via oriented attachment in long chain alkylamine solvents. Here, we report a new synthesis method to make novel Y_2O_3 nanoparticles with a square platelet morphology. Although there are many reports on the synthesis and upconversion properties of yttrium oxide nanoparticles, there are few reports on the cytotoxicity or biocompatibility responses of nanoparticles varying morphology [38, 63]. We characterize the samples by a variety of techniques, and then use these nanoparticles to assess in vitro cytotoxicity, in order to study which nanoparticle characteristics govern cytotoxicity in this system.

Experimental Design and Methods

In order to determine the nanoparticle characteristics that affect in vitro biocompatibility of Y_2O_3 nanoparticles, various nanoparticles of Y_2O_3 were synthesized as detailed in the following paragraphs ("Nanoparticle Synthesis"). The as-synthesized nanoparticles were then characterized ("Nanoparticle Characterization"), and aqueous suspensions of the nanoparticles for cytotoxicity testing were prepared and characterized ("Aqueous Nanoparticle Suspension Characterization"). Table 1 summarizes reaction conditions used and observed characteristics. Finally, the nanoparticles were tested for cytotoxicity with cells and ROS generation ("Cell Studies").

Nanoparticle Synthesis

Yttrium (III) acetate hydrate 99%, technical grade oleylamine 70%, reagent grade ammonium hydroxide 30%, yttrium (III) nitrate hexahydrate 99.8%, ethylene glycol anhydrous 99.8%, reagent grade ethanol 99.5%, reagent grade methanol 99.8%, reagent grade chloroform 99.8%, and reagent grade hexanes 98.5% were all purchased from Sigma–Aldrich (St. Louis, MO) and used without further purification.

Square platelets and spherical nanoparticles were synthesized by a modification of the solvothermal decomposition method developed by Si et al. [56]. In a standard synthesis, 0.5 mmol of yttrium acetate was dissolved in 30-mL oleylamine in a three-neck flask. The solution was stirred and degassed under vacuum at ~70 °C until bubbling stopped, typically 5–10 min. The degassed solution was then rapidly heated to 310 °C. At approximately 150 °C, the clear yellow solution turned cloudy white, indicating the nucleation of nanoparticles. The solution was held at 310 °C for 30 min, after which an ~ 5 mL aliquot (referred to as A1, spherical nanoparticles) was then removed from the solution to follow morphological evolution of the nanoparticles. Subsequently, an additional 0.5 mmol of yttrium acetate dissolved in 5-mL oleylamine was slowly dripped in to the solution at a rate of 1 mL/min. Immediately after all solution had dripped in, a second ~5 mL aliquot (A2) was removed. The reaction was allowed to continue for 15 min, after which a third aliquot of ~5 mL (A3) was removed. The reaction was allowed to proceed for an additional 15 min (product, platelets), after which heating was stopped. Nanoparticles were kept in the reaction solution and precipitated and washed as needed. The washing method depended upon the characterization technique employed, as detailed in the section "Nanoparticle Characterization".

To have an additional nanoparticle morphology for cytotoxicity testing, Y_2O_3 nanoparticles of rod-like morphology were synthesized hydrothermally in ethylene glycol in water solvent mixture by a previously published method reported by Yin et al. [47]. Briefly, 150 mL of 0.2 M $Y(NO_3)_3$ aqueous solution was added to 200 mL of ammonium hydroxide. The resulting precipitate was centrifuged at ~6,000 RCF (Relative Centrifugal Force) for 5 min and washed with water 3 times, then resuspended in

Table 1 Nanoparticle characteristics and measurement methods

Measurement	Sample 1	Sample 2	Sample 3
TEM			
Morphology	Spheres	Platelets	Rods
Size (nm)	5	140	30 × 150
XRD			
Phase	Cubic	Cubic	Cubic
Crystallite size (nm)	3	4	11
BET			
Surface area (m^2/g)	150	109	93
Size (nm), spherical shape factor	8	11	13
Size (nm), morphology shape factor	8, 6	24, 8.6	45, 25
Carbon analysis (wt%)	3.13	11.45	1.68
Ligand coverage (molecules/nm^2)	0.6	3	5
Zeta potential (mV)	−13	−27	−28
DLS (μm) volume weighted mean	~1.5	~1.5	~1.5
SLS (μm) volume weighted mean	0.7	0.7	0.8

Sample 1 refers to the solvothermally synthesized nanoparticles, Sample 2 refers to solvothermally synthesized nanoparticles with precursor additions, and Sample 3 refers to hydrothermally synthesized nanoparticles

60 mL of ethylene glycol. The solution was placed into a Teflon liner and hydrothermally reacted in a 160-mL Parr bomb Series 4760 filled to 80% volume capacity (Parr Instrument Co., Moline, IL) for 5 h at 250 °C. The reaction product was precipitated and washed as described earlier.

Nanoparticle Characterization

To study size and morphological evolution of the nanoparticles prepared by solvothermal and hydrothermal methods, transmission electron microscopy (TEM) was employed. To prepare TEM samples, nanoparticles were precipitated from the reaction solution by centrifugation at ~6,000 RCF for 5 min (Beckman Coulter Avanti J-26 XP, Fullerton, CA), then washed by resuspension in ethanol and precipitated by centrifugation at ~3,000 RCF for 5 min. The precipitate was resuspended in chloroform or hexanes, and the solution was diluted until no longer turbid. A drop of dilute nanoparticle suspension was deposited onto a 400-mesh Formvar-backed carbon grid (Electron Microscopy Sciences, Hatfield, PA), dried at room temperature under vacuum for 24 h, and imaged at 125 kV with a JEOL 100cX TEM (Tokyo, Japan).

To study crystal phase, X-ray diffraction (XRD) was performed. Nanoparticles were precipitated from the reaction solution and washed as described earlier for TEM characterization. The washing was repeated 3 times, then samples were dried at room temperature under vacuum (BOC Edwards RV 8, Tewksbury, MA) for approximately 1 h, until the powder appeared free flowing. The dried powder was placed onto a glass slide with a thin layer of vacuum grease (Dow Corning High Vacuum Silicone Grease, Sigma–Aldrich, St. Louis, MO). XRD spectra were taken on a Kristalloflex D500 (Siemens Analytical Instrument Inc., Madison, WI), with a scan range of 25–65 for 2θ, step size of .02°, and dwell time of 1.5 s. Powder Diffraction File (PDF) reference JCPDF No. 41-1105 was taken from the libraries of the International Center for Diffraction Data (ICDD, Newtown Square, PA). Crystallite size was estimated from XRD peak broadening using the Scherrer calculation [64]:

$$d = \frac{0.9\lambda}{B\cos\theta_B}$$

where d is crystallite diameter, λ is the wavelength of the X-rays, B is the peak breadth of the XRD peak, and θ_B is the Bragg angle (in radians). B and θ_B were determined by fitting the peaks in the XRD spectra with Gaussian and Lorentzian peaks using Origin 7.5 software (OriginLab Corp, Northampton, MA). Reported sizes were averaged from the sizes calculated using each peak fit across all distinguishable peaks in the XRD spectrum.

Nitrogen isotherms were used to determine nanoparticle surface area. Nanoparticles were precipitated from the reaction solution and washed as described earlier for TEM characterization. The washing was repeated 2 times, then samples were washed with methanol 2 times, and then with acetone 2 times. Samples were dried as described earlier for XRD measurements, then degassed at 200 °C under nitrogen (Micromeritics FlowPrep 060, Norcross, GA) for 1 h. Nitrogen adsorption isotherms were performed with a Micromeritics Gemini 2375. To ensure that the degassing procedure did not affect particle size, samples were scanned again with XRD following nitrogen isotherms to check for peak sharpening. Surface area was calculated from nitrogen isotherms using the Brunauer–Emmet–Teller (BET) equation [65]. A calculated volume to area–weighted particle size, D, (particle diameter or side length for non-spherical morphologies) was determined from specific surface area using the relationship [66]:

$$D = K_s/\rho S_{\mathrm{BET}}$$

where K_s is the particle shape coefficient, ρ is particle density, and S_{BET} is the specific surface area. K_s is defined as [66]:

$$K_s = D_e A/V$$

where D_e is an equivalent diameter of a sphere with the same volume as the particle, A is the surface area of the particle, and V is the volume of the particle. A theoretical density value for single crystalline cubic Y_2O_3 of 5.028 [67] was used for calculations. As density has been shown to decrease as particle size moves to the nanoscale domain, a calculated nanoparticle density based on a core/shell model was also used for comparison [68].

Fourier Transform Infrared Spectroscopy (FT-IR) was performed to probe the chemical nature of the nanoparticle surface. For FT-IR measurements, nanoparticles were precipitated from the reaction solution and washed as described for nitrogen isotherms. Samples were dried as described earlier for XRD measurements. Diffuse transmission FT-IR spectra for the powders were recorded at room temperature with a Galaxy Series 5000 FT-IR (Madison Instruments Inc., Middleton, WI).

To determine the amount of water or oleylamine remaining on washed and dried nanoparticle powders, thermogravimetric analysis (TGA) was performed, as well as carbon analysis. Nanoparticles were precipitated from the reaction solution and washed as described earlier for nitrogen isotherms. Samples were dried as described earlier for XRD measurements. TGA was performed with a Perkin Elmer TGA 7 LoTemp (Perkin Elmer, Waltham, MA) under air flowing at a rate of 20 mL/min. Samples were heated from room temperature to 100 °C and held at this temperature for 90 min, then ramped to 800 °C at a rate of

25 °C/min and held for 90 min at 800 °C. Carbon analysis by combustion was conducted by Robertson Microlit Laboratories, Madison, NJ.

Aqueous Nanoparticle Suspension Characterization

Nanoparticle stock suspensions were prepared by washing and drying nanoparticle samples as described earlier for TGA, and dispersing a known weight of nanoparticles in deionized water via ultrasonication (Fisher Scientific Ultrasonicator FS60, Pittsburgh, PA) for 45 min, to achieve a concentration of 10 mg/mL. These stock suspensions were used for characterization and testing as described later. Because the as-synthesized nanoparticles dispersed poorly in water and tended to agglomerate, if the stock suspensions had been sitting for more than a day, they were sonicated for 30 min immediately prior to any testing. No surface modification was performed in order to test the cytotoxicity of native nanoparticles without convoluting effects from surface functionalization. Agglomerate size was measured using dynamic light scattering (Brookhaven Instruments Zetapals Particle Size Analyzer, Holtsville, NY; 3 scans, 3 runs/scan, 60 s/run) and static light scattering (Beckman Coulter, Coulter LS 230, Fullerton, CA, 3 runs, 60 s/run). Zeta potential was calculated from electrophoretic mobility determined via phase analysis light-scattering measurements with a Brookhaven Instruments Zetapals Particle Size Analyzer using the Smoluchowski model [69] (Holtsville, NY, 3 scans, 3 runs/scan, 30 s/run).

Cell Studies

Human foreskin fibroblasts (HFF) were isolated from circumcision samples and expanded. Fibroblast cells were chosen for cellular tests because they are a widely accepted model cell type used for cytotoxicity testing [70]. Cells were grown in T25 (Becton–Dickson, Franklin Lakes, NJ) or T75 flasks (Corning Corp., Corning, NY) with McCoy's 5A Media (Gibco, Carlsbad, CA) supplemented with 1% L-glutamate (Invitrogen, Carlsbad, CA), 10% fetal bovine serum (Gibco, Carlsbad, CA), and 1% penicillin–streptomycin (Lonza, Walkersville, MD). For cytotoxicity testing, cells were passaged with Trypsin–EDTA (Lonza, Walkersville, MD) and reseeded into 96-well tissue culture polystyrene plates (Becton–Dickson, Franklin Lakes, NJ). Cells were allowed to attach and grow to ~80–90% confluency (density) for cytotoxicity testing. Nanoparticle test suspensions were prepared by diluting an appropriate volume of stock suspension in complete media to achieve desired testing concentrations (from 25 to 500 μg/mL).

For cytotoxicity tests, media was removed from cells plated in 96-well plates and replaced with nanoparticle-enriched media. At least 6 replicates per sample were tested. After 24 h, wells were washed with PBS and stained with calcein AM (Invitrogen, LIVE/DEAD Cytotoxicity Kit for Mammalian Cells, Carlsbad, CA). Non-fluorescent calcein AM enters the cells, and is converted to fluorescent calcein in the presence of esterase activity, thus staining only live cells. Cells were also stained with ethidium homodimer (Invitrogen, LIVE/DEAD Cytotoxicity Kit for Mammalian Cells, Carlsbad, CA), which cannot penetrate intact cell membranes, thus staining only dead cells. Due to washing steps conducted before the assay, most dead cells were washed off the wells, rendering the readings of the ethidium homodimer stain similar for all test conditions and controls. Therefore, only the calcein fluorescence data were used. Plates were read on a fluorescent plate reader (Applied Biosystems, Cytofluor Series 4000, Foster City, CA). Microsoft Excel was used to perform *t*-testing for statistical analysis of the data.

Reactive oxygen species (ROS) generation of the nanoparticles without cells was tested by adding dichlorofluorescein diacetate (Sigma–Aldrich, St. Louis, MO) to 100 μg/mL of nanoparticles in PBS. When non-fluorescent dichlorofluorescein diacetate becomes oxidized, it becomes fluorescent. Sample fluorescence was read with a fluorescence plate reader (Applied Biosystems, Cytofluor Series 4000, Foster City, CA).

Results and Discussion

Characterization of Nanoparticles

In order to understand the underlying nanoparticle characteristics that are responsible for cytotoxicity in a given system of nanoparticles, thorough characterization of the nanoparticle samples is key. Therefore we employed a variety of characterization methods to study the particle size, morphology, phase, crystallite size, surface chemistry and area, and agglomeration of the different nanoparticle samples in aqueous solution. It is important to not only characterize the nanoparticle powders, but to also characterize the nanoparticles in aqueous solution, as the samples must be in aqueous solution for cytotoxicity testing.

TEM images of the solvothermal reaction product (Fig. 1) show novel square platelet morphology. Based on the SAED we performed (data not shown), the appearance of ring patterns indicates that the particles are polycrystalline. The darker contrast areas that appear linear indicate edges of the thin squares that have begun to curl over or overlap. Platelets range from 140 to 160 nm per side. To study the morphological evolution of these nanocrystals, TEM of the various aliquots removed during different points of the synthesis (as described in the "Experimental Design and Methods"), A1–A3, was performed (Fig. 2).

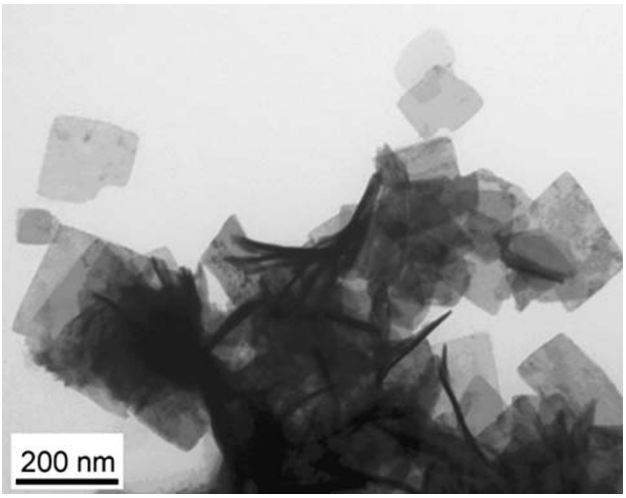

Fig. 1 TEM image of final solvothermal product after more precursor added; square platelets ranging 140–160 nm per side

After 30 min of heating at 310 °C, before additional precursors are dripped in (A1), the nanoparticles are spherical (spherical nanoparticles) and have diameters ranging from 4 to 8 nm. Immediately after additional precursors are dripped in (A2), the nanoparticles appear to aggregate and begin to form tangles of wire-like structures. No square platelets are present at this stage in the reaction. Fifteen minutes after additional precursors have been dripped in (A3), flat ribbons and a few isolated square platelets are seen. These ribbons appear to be comprised of aggregates of nanoparticles. After 30 min, only square platelets are found. The TEM image of the Y_2O_3 nanoparticles synthesized via the solvothermal method [47], Fig. 3, shows clumps of individual nanoparticles with rod-like morphology of $\sim$150–200 nm in length and $\sim$33 nm diameter. Aspect ratios for the rods range from 4.5 to 6.0.

Oriented attachment of spherical nanoparticles into nanorods has been noted before for yttrium oxide [59]. Zhang et al. [59] report monodisperse Y_2O_3 nanoparticles that form chain-like agglomerates due to van der Waals interactions, which then cement and reshape into nanorods. A similar mechanism can be used to explain the morphological evolution of the square nanoplatelet presented here. First, spherical nanoparticles form, (Fig. 2a), which then agglomerate into a tangle of wires upon the addition of more precursors into the reaction solution (Fig. 2b). These then begin to grow laterally, producing ribbons (Fig. 2c). These intermediate morphologies were not chosen for cytotoxicity testing due to their large (order of microns) length scales, and the fact that they are comprised of associated individual spherical nanoparticles. The

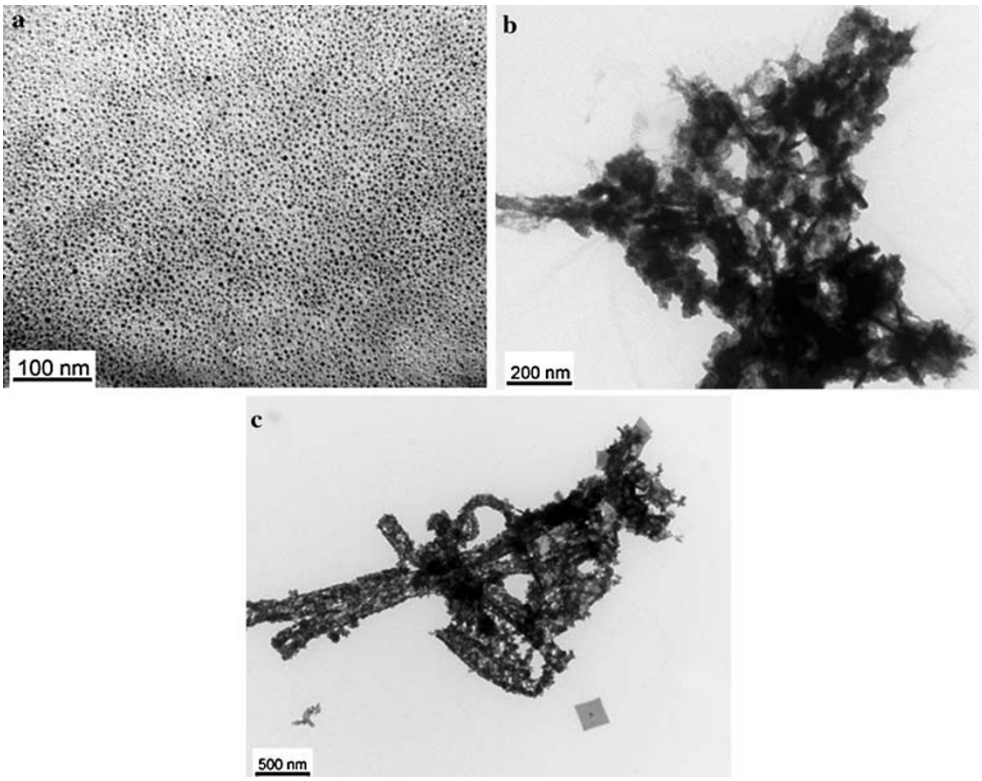

Fig. 2 **a** TEM image of 30 min reaction aliquot A1. **b** TEM image of aliquot A2, immediately after more precursor addition. **c** TEM image of aliquot A3, 15 min after more precursor addition

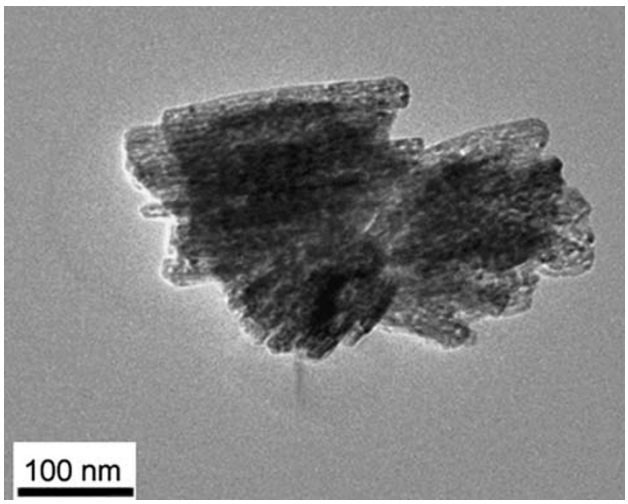

Fig. 3 TEM image of hydrothermal Y_2O_3 nanoparticles

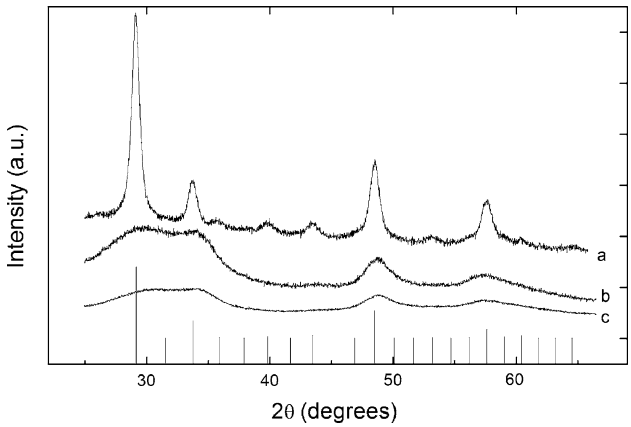

Fig. 4 XRD spectra of Y_2O_3 nanoparticles: **a** rod-like sample, **b** platelets, **c** 5-nm spherical nanoparticles. *Vertical black lines* correspond to standard cubic Y_2O_3, PDF # 41-1105

interactions that cause the nanoparticles to agglomerate into the observed transitional morphologies during the reaction are not strong enough to keep the morphologies stable in the presence of many charged species, as found in cell culture conditions. The spherical nanoparticles that comprise the ribbon structures then coalesce and reform into square platelets or sheets. Wang et al. have noticed the formation of Lu_2O_3 [71, 72] square platelets from spherical nanoparticles under hydrothermal conditions. The addition of more precursors was crucial for the square platelet morphology. If the reaction was carried on for 1 h at 310 °C without addition of more precursors, only spherical nanoparticles formed. Furthermore, if precursors were dripped into the solvent at 310 °C without any existing precursors present, only spherical nanoparticles formed.

The XRD spectra of the samples, Fig. 4, are shown together with the cubic standard (*Ia3*, JCPDF No. 41-1105, vertical lines). The XRD spectra of the platelets and of the spherical nanoparticles show very broad diffraction peaks, which is a result of the small size of the nanoparticles. Although the lateral dimensions of the platelets are ~120 nm, their thickness is on the order of a few nanometers, so considerable peak broadening is observed with this sample as well. The spectrum of the rod-like nanoparticle sample shows decidedly less broadening. Peak broadening due to small size has been observed in other reports of Y_2O_3 nanoparticles [63]. The choice of precursor is important for the resulting product phase, as Si et al. [56] reported that yttrium acetylacetonate could not be converted into cubic Y_2O_3 in pure oleylamine.

Crystallite sizes calculated from the peak broadening, listed in Table 1, were 3 nm for the spherical nanoparticle sample, 4 nm for the platelet sample, and 11 nm for the rod-like sample. Discrepancies between TEM and XRD calculated sizes of particles can be due to differences in size distributions captured by the different techniques, as well as polycrystallinity of the particles. Based on our SAED (discussed earlier), the size discrepancy here appears due to the polycrystalline nature of the platelet and rod-like particles. Additionally, the differences in sizes (e.g., 33 nm diameter and 150–200 nm length for rods as measured via TEM vs. XRD calculated size of 11 nm) are too large to be attributed to differences in size distributions. The fact that these particles are polycrystalline means they are comprised of randomly oriented crystallites, and there is no preferred crystallographic orientation, which could possibly be the case if the rod or platelet particles were single crystals.

The surface area as determined by nitrogen isotherms was 150 m^2/g for the spherical nanoparticles, 109 m^2/g for the platelet sample, and 93 m^2/g for the rod-like nanoparticles. Due to the large dimensions of the rods, this sample has the smallest specific surface area, while the 5-nm spherical nanoparticles have the largest specific surface area because of their small size. XRD of the samples, post-degassing, did not exhibit any reduction in peak broadening, indicating that the degassing procedure did not cause significant crystal growth. Particle size (see Table 1) calculated from the specific surface area, using the single crystal density value of 5.028, with a shape factor (K_s) of 6 (spherical), was 8 nm for the spherical nanoparticles, 11 nm for the platelet sample, and 13 nm for the rod-like nanoparticles. Accounting for non-spherical morphologies by using a calculated K_s of 8.6 (aspect ratio = 5) for the rods and 25 (aspect ratio = 28) for the platelets gives a calculated particle size of 18 and 45 nm, respectively. These particle sizes are still significantly smaller than those observed via TEM (150 and 140 nm, respectively), indicating that perhaps the single crystal density value is not an appropriate choice for these particles; therefore, particle sizes were calculated using a calculated density value obtained by assuming a core of yttrium oxide and a shell (surface) layer of oleylamine through a model developed

by Lojkowski [68]. The model gives sizes closer to those seen with TEM (e.g., 70 nm for the platelet), indicating that the samples probably have a lot of ligand present, reducing their density. The sizes are still not reconcilable, though, which can be due to particle size distributions not seen via TEM and not knowing the precise particle density considering how organics coat the particle surfaces.

FT-IR data indicate that the spherical nanoparticle and platelet samples are coated with a "shell" of oleylamine. Peaks are observed at ca 2,930 and 2,850 cm^{-1}, corresponding to C–H stretching, and peaks at ca 1,060, 950 cm^{-1} corresponding to =C–H out of plane and in plane bending [73] or NH_2 bending modes [74]. All match the spectra of pure oleylamine. In contrast, the rod-like sample coated with ethylene glycol has a broad OH peak ca 3,375 cm^{-1} and a C–H stretch of 2,830 cm^{-1} and asymmetric and symmetric glycolate stretches (less like C–H bends) at 1,380 and 1,620 cm^{-1} [75]. These FT-IR results are as expected; samples synthesized in oleylamine are coated with oleylamine, and the sample synthesized in ethylene glycol is coated with ethylene glycol.

Zeta potentials for all aqueous nanoparticle suspensions were highly negative, with spherical nanoparticles having an average zeta potential of −13 mV, the platelets having an average zeta potential −27 mV, and the rods having an average zeta potential −28 mV. The volume weighted mean agglomerate size of all aqueous nanoparticle suspensions as measured by dynamic light scattering was $\sim 1.5\mu$. However, this size is actually beyond the range of sizes than can reliably be determined with dynamic light scattering. Therefore, static light scattering was performed for a more accurate determination of agglomerate size. As determined from static light scattering, the volume weighted mean size for the spherical nanoparticles was 0.7 μm, the platelet sample was 0.7 μm, and the rod-like sample was 0.8 μm. This agglomerate size is larger than seen in the TEM images, but this is to be expected, as the TEM samples were prepared from nanoparticles suspended in organic solvents, where they disperse much better.

The weight losses seen in the TGA profile, shown in Fig. 5, can correspond to the loss of organic species and water from the nanoparticle samples. The rod-like sample had a weight loss of approximately 3 wt%, the spherical nanoparticles a weight loss of approximately 25 wt%, and the platelet sample a weight loss of approximately 32 wt%. Carbon analysis was used to determine the weight percentage of carbon for each sample. The results show that the platelet sample contained 11.5 wt% carbon, the spherical nanoparticle sample was comprised of approximately 3.13 wt% carbon, and the rod-like sample was approximately 1.68 wt% carbon. This indicates a significantly elevated level of organic ligand present in the platelet sample when compared to the other samples. The approximate

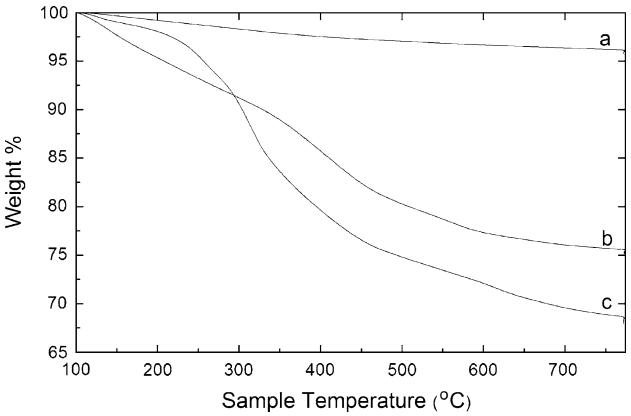

Fig. 5 TGA traces of Y_2O_3 nanoparticles: **a** rods, **b** 5-nm spherical nanoparticles, **c** platelets

ligand coverage (molecules per area), calculated from the carbon analysis data and the surface area measurements, was found to be 0.6 molecules of oleylamine per nm^2 for the spherical sample, 3 molecules of oleylamine per nm^2 for the platelet sample, and 5 molecules of ethylene glycol per nm^2 for the rod-like sample. The difference in site density of the ligand for spherical nanoparticles when compared to the platelet and rod samples may be due to a difference in the packing of the ligand on a highly curved surface such as the small spherical nanoparticles, when compared to the packing of the ligand on more planar surfaces like the platelets or the larger rods. The difference may also be due to the polycrystalline nature of the platelet and rod-like samples. Based on the weight percentage of carbon per sample, the additional weight percent loss due to hydrogen, nitrogen (for oleylamine only), and oxygen (for ethylene glycol only) from the respective surface modifying ligand can be calculated. Subtracting the total weight percent loss due to the ligand from the TGA data gives a remaining weight loss of approximately 17.5 wt% for the platelet sample, 21 wt% for the spherical nanoparticles, and no remaining weight loss for the rod sample. These weight losses can be due to the loss of water. FT-IR supports this, as a broad OH band is observed in the spectra of the nanoparticle samples. Although this seems to be a relatively high water content for samples synthesized from non-aqueous solvents, the water is probably due to the water from the yttrium nitrate hexahydrate and insufficient drying of the nanoparticles (approximately 1 h under vacuum at room temperature) after washing with ethanol and methanol. Water content of approximately 12 wt% has been reported even for ZnO nanoparticle samples dried at 100 °C for 24 h [76].

In summary, the characterization data (Table 1) establish that the nanoparticle samples are of similar crystal phase, crystallite size, zeta potential, and agglomerate size in aqueous media and that the platelet and rod-like samples are polycrystalline. The particles differ in surface area,

morphology, particle size, amount of ligand present per weight of sample, and degree of ligand coverage. Once the characteristics of the nanoparticle samples were studied, samples were then tested for cytotoxicity with cells, with the goal of assessing the nanoparticle characteristics that affect cytotoxicity.

Cytotoxicity and ROS Generation of Nanoparticles

Nanoparticles were tested for in vitro cytotoxicity by conducting a LIVE/DEAD assay, and assaying the amount of ROS generated by the particles. Figure 6 shows the normalized viability of cells treated with different nanoparticle samples with concentrations ranging from 25 to 500 μg/mL, and then stained with calcein AM. Cell viability is effectively invariant for the various concentrations of Y_2O_3 spherical nanoparticles, with no statistically significant difference between the treated samples and the control. For the rod-like sample, at concentrations of 100 μg/mL and above, cell viability is increased in a statistically significant manner, approximately 1.3–1.5 times the untreated control, as indicated with asterisks. There are various reports noting enhanced proliferation of cells exposed to inorganic nanoparticles such as europium hydroxide [77] or strontium-doped calcium polyphosphate [78], although the exact mechanism is not known. Similarly, the yttrium oxide rods may be enhancing HFF proliferation. Further work is required to understand this phenomenon in depth. For the cells incubated with Y_2O_3 platelets, viability decreases in a statistically significant manner with increasing concentrations of nanoparticles. At the lowest dose of 25 μg/mL, cells exhibit viability similar to the untreated control. However, at 50 μg/mL, viability is decreased to approximately 75%, and at concentrations of 75 μg/mL and above, viability is only ~25%.

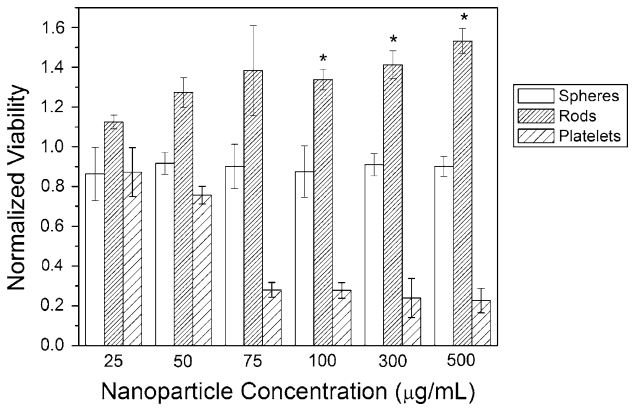

Fig. 6 Viability of HFF cells (normalized to a non-treated control sample) after 24 h exposure to various nanoparticle samples. *Asterisked samples* represent samples with a statistically significant (at $\alpha = .05$ level) increase in viability above control (p values are .000517, .000178, and 5.44×10^{-5}, respectively)

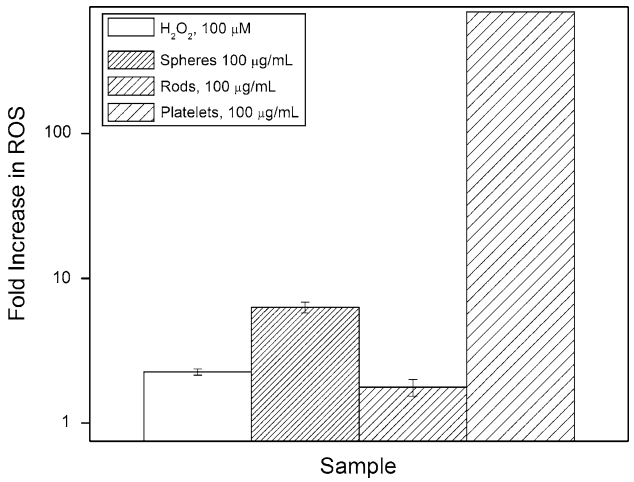

Fig. 7 Increase of ROS species detected with dichlorofluorescein diacetate compared to PBS control

The generation of reactive oxygen species (ROS) from nanoparticles is a common contributing factor to nanoparticle cytotoxicity [16, 24, 79, 80]; therefore, to better understand the observed response of the cells to the different nanoparticle samples, the nanoparticles were tested without cells to determine their role in generation of ROS. Figure 7 shows ROS generation of nanoparticle samples in PBS, normalized to the fluorescence reading of PBS alone (set as 1). The results indicate that in PBS, the nanoparticles generate significant levels of ROS. The rod-like sample generates levels of ROS comparable to those generated by 100 μM hydrogen peroxide, approximately 1.8, while the spherical nanoparticles generate approximately 3.5 times the level (~6.3), and the platelets generate an extremely high level (~ 690). From the ROS generation results, the observed cytotoxicity of the platelet-shaped nanoparticles can be attributed, at least in part, to the increased level of ROS generated by this sample, which is significantly higher than that generated by the other samples.

Determining the source of the observed differences in ROS generation and cytotoxicity requires a careful analysis of the characterization data. One would expect the ROS generation and cytotoxicity to correlate to a surface characteristic of the nanoparticles (area, chemistry, etc.), as the surface of the nanoparticles is what is exposed to cells and what is available to react and form ROS. Based on the characterization data, ROS levels surprisingly do not correlate with specific surface area, as the spherical sample possessed the largest specific surface area but did not generate the highest levels of ROS. It is also clear that the ROS generation of the platelets is not a result of the particle size, as the rod-like nanoparticles possess similar lengths but did not generate as much ROS. Both the platelet and rod-like samples are polycrystalline, and as such, they are comprised of randomly oriented crystallites

without preferred crystallographic orientation. Therefore, the surface of these particles, aside from the capping ligand, is similar, and cannot be the cause of the observed cytotoxicity response. Additionally, agglomerate size in aqueous solution, zeta potential, and crystal phase of all samples were similar, so these characteristics cannot be affecting ROS generation levels. The most significant difference between samples that can be correlated to the ROS generation and cytotoxicity is the surface chemistry of the samples. The platelet sample has elevated levels of surface coverage of oleylamine relative to the spherical sample, as calculated from the carbon analysis and surface area data. Although the rod-like sample had a higher level of surface coverage, it is coated with ethylene glycol, which is seemingly less toxic to cells than oleylamine [81]. The characterization data therefore seem to point to the oleylamine in the platelet sample as the cause of the observed cytotoxicity.

Conclusions

In conclusion, we have synthesized and characterized yttrium oxide nanoparticles of spherical, platelet, and rod-like morphology, and explored the cytotoxicity of these different nanoparticles. Spherical nanoparticles had no effect on cell viability up to the maximum tested concentration of 500 μg/mL, and rods enhanced cell proliferation at concentration of 100 μg/mL and above. Platelets were cytotoxic to HFF cells at concentrations of 50 μg/mL and above, which in part may be due to the increased ROS generation observed from this sample. Based on the nanoparticle characterization, the increased ROS generation is attributed to the stabilizing ligand oleylamine, which has a higher degree of surface coverage in the platelet sample than the spherical sample. While the rod-like sample had a degree of surface coverage similar to the platelets, it was coated with ethylene glycol, not oleylamine. Therefore, in this system, the surface chemistry of the nanoparticles is the characteristic that appears to govern the cytotoxicity responses. These cytotoxicity results also indicate that it is important to thoroughly characterize nanoparticle samples by a variety of methods in order to understand and properly correlate observed cytotoxicity with the correct nanoparticle characteristic. Once the true underlying nanoparticle characteristic giving rise to the observed cellular response has been determined, it may be possible to tune cytotoxicity by adjusting, either during or post-synthesis, the nanoparticle characteristic that has been pinpointed.

Acknowledgments This work was supported in part by the National Science Foundation NIRT Grant 0609000 and in part by Grant Number T32EB005583 from the National Institute Of Biomedical Imaging And Bioengineering. The content is solely the responsibility of the authors and does not necessarily represent the official views of the National Institute Of Biomedical Imaging And Bioengineering or the National Institutes of Health.

References

1. K.S. Soppimath, T.M. Aminabhavi, A.R. Kulkarni, W.E. Rudzinski, J. Control. Release **70**, 1 (2001)
2. J. Kreuter, Adv. Drug Deliv. Rev. **47**, 65 (2001)
3. J.D. Hood, M. Bednarski, R. Frausto, S. Guccione, R.A. Reisfeld, R. Xiang, D.A. Cheresh, Science **296**, 2404 (2002)
4. H.Q. Mao, K. Roy, V.L. Troung-Le, K.A. Janes, K.Y. Lin, Y. Wang, J.T. August, K.W. Leong, J. Control. Release **70**, 399 (2001)
5. Y.I. Chung, G. Tae, S.H. Yuk, Biomaterials **27**, 2621 (2006)
6. X.H. Gao, Y.Y. Cui, R.M. Levenson, L.W.K. Chung, S.M. Nie, Nat. Biotechnol. **22**, 969 (2004)
7. M.E. Akerman, W.C.W. Chan, P. Laakkonen, S.N. Bhatia, E. Ruoslahti, Proc. Natl. Acad. Sci. USA **99**, 12617 (2002)
8. X.H. Gao, L.L. Yang, J.A. Petros, F.F. Marshal, J.W. Simons, S.M. Nie, Curr. Opin. Biotechnol. **16**, 63 (2005)
9. I. Roy, T.Y. Ohulchanskyy, H.E. Pudavar, E.J. Bergey, A.R. Oseroff, J. Morgan, T.J. Dougherty, P.N. Prasad, J. Am. Chem. Soc. **125**, 7860 (2003)
10. S. Mornet, S. Vasseur, F. Grasset, E. Duguet, J. Mater. Chem. **14**, 2161 (2004)
11. C. Kirchner, T. Liedl, S. Kudera, T. Pellegrino, A. Javier, H. Gaub, S. Stolzle, N. Fertig, W. Parak, Nano Lett. **5**, 331 (2005)
12. A. Derfus, W. Chan, S.N. Bhatia, Nano Lett. **4**, 11 (2004)
13. W.H. Chan, N.H. Shiao, P.Z. Lu, Toxicol. Lett. **167**, 191 (2006)
14. L.E. Rikans, T. Yamano, J. Biochem. Mol. Toxicol. **14**, 110 (2000)
15. S.J. Cho, D. Maysinger, M. Jain, B. Roder, S. Hackbarth, F.M. Winnik, Langmuir **23**, 1974 (2007)
16. T. Xia, M. Kovochich, J. Brant, M. Hotze, J. Sempf, T. Oberley, C. Sioutas, J. Yeh, M. Wiesner, A. Nel, Nano Lett. **6**, 1794 (2006)
17. Z. Markovic, V. Trajkovic, Biomaterials **29**, 3561 (2008)
18. W. Lin, Y. Huang, X. Zhou, Y. Ma, Int. J. Toxicol. **25**, 451 (2006)
19. A. Verma, O. Uzun, Y.H. Hu, Y. Hu, H.S. Han, N. Watson, S.L. Chen, D.J. Irvine, F. Stellacci, Nat. Mater. **7**, 588 (2008)
20. P. Leroueil, S. Hong, A. Mecke, J. Baker, B. Orr, M. Holl, Acc. Chem. Res. **40**, 335 (2007)
21. C.W. Lam, J.T. James, R. McCluskey, R.L. Hunter, Toxicol. Sci. **77**, 126 (2004)
22. D.B. Warheit, B.R. Laurence, K.L. Reed, D.H. Roach, G.A.M. Reynolds, T.R. Webb, Toxicol. Sci. **77**, 117 (2004)
23. J. Lovric, H. Bazzi, Y. Cuie, G. Fortin, F.M. Winnik, D. Maysinger, J. Mol. Med. **83**, 377 (2005)
24. T. Xia, M. Kovochich, M. Liong, L. Madler, B. Gilbert, H. Shi, J. Yeh, J. Zink, A. Nel, ACS Nano. **2**, 2121 (2008)
25. C. Sayes, R. Wahi, P. Kurian, Y. Liu, J. West, K. Ausman, D.B. Warheit, V. Colvin, Toxicol. Sci. **92**, 174 (2006)
26. G. Jia, H. Wang, L. Yan, X. Wang, R. Pei, T. Yan, Y. Zhao, X. Guo, Environ. Sci. Technol. **39**, 1378 (2005)
27. L. Ding, J. Stilwell, T. Zhang, O. Elboudwarej, H. Jiang, J. Selegue, P. Cooke, J. Gray, F.F. Chen, Nano Lett. **5**, 2448 (2005)
28. S. Wang, W. Lu, O. Tovmachenko, U.S. Rai, H. Yu, P.C. Ray, Chem. Phys. Lett. **463**, 145 (2008)
29. A. Elder, H. Yang, R. Gwiazda, X. Teng, S. Thurston, H. He, G. Oberdorster, Adv. Mater. **19**, 3124 (2007)
30. D.B. Warheit, P. Borm, C. Hennes, J. Lademann, Inhal. Toxicol. **19**, 631 (2007)

31. M.L. Chang, S.L. Tie, Nanotechnology **19**, 075711 (2008)
32. C.G. Morgan, A.C. Mitchell, Biosens. Bioelectron. **22**, 1769 (2007)
33. T. Koishi, M. Yamada, K. Soga, D. Matsuura, Y. Nagasaki, J. Photopolym. Sci. Tech. **19**, 145 (2006)
34. D. Matsuura, Appl. Phys. Lett. **81**, 4526 (2002)
35. J.A. Capobianco, F. Vetrone, J.C. Boyer, A. Spenghini, M. Bettinelli, J. Phys. Chem. B. **106**, 1181 (2002)
36. J.A. Capobianco, F. Vetrone, T. D'Alesio, G. Tessari, A. Spenghini, M. Bettinelli, Phys. Chem. Chem. Phys. **2**, 3202 (2000)
37. J. Frangioni, Curr. Op. Chem. Biol. **7**, 626 (2003)
38. D. Schubert, R. Dargush, J. Raitano, S.W. Chan, Biochem. Biophys. Res. Comm. **342**, 86 (2006)
39. B. Guo, Z. Luo, J. Am. Ceram. Soc. **91**, 1653 (2008)
40. J. Mouzon, M. Oden, Powder Technol. **177**, 77 (2007)
41. S. Mukherjee, V. Sudarsan, R.K. Vasta, S.V. Godbole, R.M. Kadam, U.M. Bhatta, A.K. Tyagi, Nanotechnology **19**, 325704 (2008)
42. A.M. Pires, O.A. Serra, M.R. Davolos, J. Lumin. **113**, 174 (2005)
43. T. Ye, Z. Guiwen, Z. Weiping, X. Shangda, Mat. Res. Bull. **32**, 501 (1997)
44. M. Inoue, H. Otsu, H. Kominami, T. Inui, J. Am. Ceram. Soc. **74**, 1452 (1991)
45. M.K. Devaraju, S. Yin, T. Sato, Nanotechnology **20**, 305302 (2009)
46. A. Martinez, J. Morales, P. Salas, C. Angeles-Chavez, L.A. Diaz-Torres, E. De la Rosa, Microelectron. J. **39**, 551 (2008)
47. S. Yin, M. Shinozaki, T. Sato, J. Lumin. **126**, 427 (2007)
48. Y. Mao, J. Huang, R. Ostroumov, K. Wang, J. Chang, J. Phys. Chem. B. **112**, 2278 (2008)
49. H. Giesche, E. Matijevic, J. Mater. Res. **9**, 436 (1994)
50. D.J. Sordelet, M. Akinc, M.L. Panchula, Y. Han, M.H. Han, J. Eur. Ceram. Soc. **14**, 123 (1994)
51. D.J. Sordelet, M. Akinc, J. Am. Ceram. Soc. **71**, 1148 (1988)
52. M. Akinc, D. Sordelet, Adv. Ceram. Mater. **2**, 232 (1987)
53. Y.S. Her, E. Matijevic, W.R. Wilcox, O.G. Bailey, G.S. Fischman, J. Mater. Sci. Lett. **11**, 1629 (1992)
54. R. Sprycha, J. Jablonski, E. Matijevic, J. Colloid Interface Sci. **149**, 561 (1992)
55. R. Bazzi, M.A. Flores-Gonzales, C. Louis, K. Lebbou, C. Dujardin, A. Brenier, W. Zhang, O. Tillement, E. Bernstein, P. Perriat, J. Lumin. **102–103**, 445 (2003)
56. R. Si, Y.W. Zhang, H.-P. Zhou, L.D. Sun, C.-H. Yan, Chem. Mater. **19**, 18 (2007)
57. R. Si, Y.W. Zhang, L.-P. You, C.-H. Yan, Angew. Chem. Int. Ed. **44**, 3256 (2005)
58. J.M. Sung, S.E. Lin, W.C.J. Wei, J. Eur. Ceram. Soc. **27**, 2605 (2007)
59. Y. Zhang, J. Guo, T. White, T. Tan, R. Xu, J. Phys. Chem. C. **111**, 7893 (2007)
60. D. Matsuura, T. Ikeuchi, K. Soga, J. Lumin. **128**, 1267 (2008)
61. H. Wang, M. Uehara, H. Nakamura, M. Iyazaki, H. Maeda, Adv. Mater. **17**, 2506 (2005)
62. G. De, W. Qin, J. Zhang, J. Zhang, Y. Wang, C. Cao, Y. Cui, Solid State Comm. **137**, 483 (2006)
63. G.K. Das, T.T. Tan, J. Phys. Chem. C. **112**, 11211 (2008)
64. B.D. Cullity, S.R. Stock, *Elements of X-ray Diffraction* (Prentice Hall, Upper Saddle River, 2001), p. 170
65. R.I. Masel, *Principles of Adsorption and Reaction on Solid Surfaces* (Wiley-IEEE, 1996), p. 301
66. P. Somasundaran, *Encylopedia of Surface & Colloid Science*, 2nd edn., 1 (Taylor & Francis, New York, 2006), p. 786
67. J. Spencer, *The Metals of the Rare Earths* (Longmans Green, London, 1919), p. 134
68. W. Lojkowski, R. Turan, A. Proykova, A. Daniszewska, Nanometrology **8**, 73 (2006)
69. E. Matijevic, M. Borkovec, *Surface and Colloid Science*, 17 (Springer, New York, 2004), p. 385
70. S.K. Bhatia, A.B. Yetter, Cell Biol. Toxicol. **24**, 315 (2008)
71. J. Wang, Q. Liu, Q. Liu, Opt. Mater. **29**, 593 (2007)
72. J. Wang, Q. Liu, Q. Liu, J. Mater. Chem. **15**, 4141 (2005)
73. M. Chen, Y. Feng, X. Wang, T.C. Li, J.Y. Zhang, D.J. Qian, Langmuir **23**, 5296 (2007)
74. M. Niasari, Z. Fereshteh, F. Davar, Polyhedron **28**, 126 (2008)
75. S.C. Chang, Y. Ho, M.J. Weaver, J. Am. Chem. Soc. **113**, 9506 (1991)
76. C. Ge, C. Xie, M. Hu, Y. Gui, Z. Bai, D. Zeng, Mater. Sci. Eng. B. **141**, 43 (2007)
77. C. Patra, R. Bhattacharya, S. Patra, N. Vlahakis, A. Gabashvili, Y. Kolypin, A. Gedanken, P. Mukherjee, D. Mukhopadhyay, Adv. Mater. **20**, 753 (2008)
78. Y.W. Chen, G.Q. Shi, Y.L. Ding, X.X. Yu, X.H. Zhang, C.S. Zhao, C.X. Wan, J. Mat. Sci. **19**, 2655 (2008)
79. A. Nel, T. Xia, L. Madler, N. Li, Science **311**, 622 (2006)
80. G. Oberdorster, E. Oberdorster, J. Oberdorster, Environ. Health Perspect. **113**, 823 (2005)
81. O.C. Wilson, E. Blair, S. Kennedy, G. Rivera, P. Mehl, Mater. Sci. Eng. C Biomim. Supramol. Syst. **28**, 438 (2008)